ACOUSTIC EMISSION DETECTION IN CONCRETE SPECIMENS: EXPERIMENTAL ANALYSIS AND SIMULATIONS BY A LATTICE MODEL

I. Iturrioz[1], G. Lacidogna[2], A. Carpinteri[2]

[1] *Federal University of Rio Grande do Sul*
Department of Mechanical Engineering
Porto Alegre, RS, Brazil

[2] *Politecnico di Torino*
Department of Structural Engineering and Geotechnics
Torino, Italy

ABSTRACT

In civil engineering, materials subjected to stress or strain states a quantitative evaluation of damage is of great importance due to the critical character of this phenomena, which at certain point suddenly turns into catastrophic failure.

An effective damage assessment criterion is represented by the statistical analysis of the Acoustic Emission (AE) amplitude distribution signals that emerges from the growing micro-cracks. The amplitudes of such signals are distributed according to the Gutenberg- Ritcher (GR) law and characterized through the *b*-value which systematically decreases with damage growth.

The *b*-value analysis was conducted on two experimental tests carried out on concrete specimens loaded up to failure. The first one is a prismatic specimen subjected to uniaxial compression load, the second one is a pre-cracked beam subjected to three point bending test.

The truss-like Discrete Element Method (DEM) was used to made numerical simulation on the experimental tests. The comparison between experimental and numerical analyses, in terms of load vs. time diagram and AE data, elaborated throughout the *b*-value and signals frequencies variations, provided results in good agreement.

Key words: Concrete; Lattice model; AE technique; *b*-value; Damage parameter.

1. INTRODUCTION

The most advanced method for a non-destructive quantitative evaluation of damage progression is the acoustic emission (AE) technique. Physically, AE is a phenomenon caused by a structural alteration in a solid material, in which transient elastic-waves due to a rapid release of strain energy are generated. AEs are also known as stress-wave emissions.

AE waves, whose frequencies typically range from kHz to MHz, propagate through the material towards the surface of the structural element, where they can be detected by sensors which turn the released strain energy packages into electrical signals Traditionally, in AE testing. a number of parameters are recorded from the signals, such as arrival time, velocity, amplitude, duration and frequency. From these parameters damage conditions and localization of AE sources in the specimens are determined, Carpinteri et. al. (2009).

Using the AE technique, an effective damage assessment criterion is provided by the statistical analysis of the amplitude distribution of the Acoustic Emission (AE) signals generated by growing microcracks. The amplitudes of such signals are distributed according to the Gutenberg-Richter (GR) law, $N(\geq A) \propto A^{-b}$, where N is the number of AE signals with amplitude $\geq A$. The exponent b of the GR law, the so-called *b*-value, changes with the different stages of damage growth: while the initially dominant microcracking generates a large number of low-amplitude AE signals, the subsequent macrocracking generates fewer signals of higher amplitude. On the other hand, the damage process is also characterized by a progressive localization identified through the fractal dimension D of the damaged domain. It may be proved that $2b=D$ (Aki(1967), Carpinteri 1994;

Turcotte (2003) ; Rundle *et al*. (2003); Carpinteri *et al*. (2008)). Therefore, by determining the *b*-value it becomes possible to identify the energy release modalities in a structural element during the AE monitoring process. The extreme cases envisaged are $D = 3.0$, which corresponds to $b=1.5$, a critical condition in which the energy release takes place through small defects evenly distributed throughout the volume, and $D=2.0$, which corresponds to $b = 1.0$, when energy release takes place on a fracture surface. In the former case diffused damage is observed, whereas in the latter case two dimensional cracks are formed leading to the separation of the structural element.

Moreover, in seismology, the energy released during an earthquake can be linked with seismogram amplitude thanks to the classical expression proposed by Ritcher (1958), $E_s \propto A^c$, where: *A* is the earthquake amplitude, and $c=[1.5, 2]$ is an exponent obtained experimentally from earthquakes measurements. Another expression appearing in a seismological context, in Chakrabarti and Benguigui (1997), is $N(>=E_s) \propto E_s^{-d}$, where *N* is the cumulative distribution of released energy and $d=[0.8, 1.1]$ is an exponent obtained from earthquakes observations.

2 RELATIONSHIP BETWEEN SIGNAL AMPLITUDE AND THE NUMBER OF AE EVENTS

Magnitude (m) is a geophysical log-scale quantity which is often used to measure the amplitude of an electrical signal generated by an AE event. Magnitude is related to amplitude (A), expressed in volts (V), by the following equation:

$$m = \text{Log } A. \tag{1}$$

The widely accepted Gutenberg–Richter (GR) law, initially proposed for seismic events, describes the statistical distribution of AE signal amplitudes :

$$N(\geq \text{A}) = \zeta A^{-b}, \tag{2}$$

where ζ and exponent *b* are coefficients that characterize the behavior of the model. We shall focus our attention on coefficient *b*.

By rewriting Eq. (2.2) as a logarithmic equation:

$$\text{Log}(N \geq \text{A}) = \text{Log } \zeta - bm, \tag{3}$$

where *N* is the number of AE peaks with magnitude greater than *m*, and coefficient *b*, referred to as ''*b*-value'', is the negative slope of the *Log N* vs. *m* diagram. Microcracks release low-amplitude AEs, while macrocracks release high-amplitude AEs. This intuitive relationship is confirmed by the experimental observation that the area of crack growth is proportional to the amplitude of the relative AE signal Pollock (1973).

From Eq. (2.3) we find that a regime of microcracking generates weak AEs, and therefore leads to relatively high *b*-values (raising the threshold *m*, gives rise to a fast decline in the number of surviving signals). When macrocracks start to appear, instead, lower *b*-values are observed.

Therefore the analysis of the *b*-value, which changes systematically with the different stages of fracture growth has been recognized as a useful tool for damage level assessment. In general terms, the fracture process moves from micro to macrocracking as the material approaches impending failure and the *b*-value decreases. While testing the materials undergoing brittle failure, the *b*-value is found to be around 1.5 in the initial stages. It then decreases with increasing stress level to ≈ 1.0 and even less as the material approaches failure:

Furthermore, as pointed out in Carpinteri et. al. (2009), the statistical analysis of *b*-values is closely correlated with the fractal geometry approach in the damage and fracture mechanics of heterogeneous materials. Fractal geometry is the natural tool to characterize self-organized processes, emphasizing their universality and the scaling laws arising at the critical points.

3. THE TRUSS-LIKE DISCRETE ELEMENT METHOD

The truss-like DEM used in this work represents the continuum by means of a periodic spacial arrangement of bars with the masses lumped at their ends. A lumped mass of ($\rho L^3/2$) corresponds to each internal node, where ρ is the density and L the length of a cubic module. The nodes will have a lumped mass of ($\rho L^3/16$) if they are localized in the corner, ($\rho L^3/8$) on the edges and ($\rho L^3/4$) on a free surface. The discretization uses a basic cubic module constructed using 20 bar elements and 9 nodes showed in Figure 1(a) and 1(b). Every node has three degrees of freedom, which are the three components of the displacement vector in the global reference system.
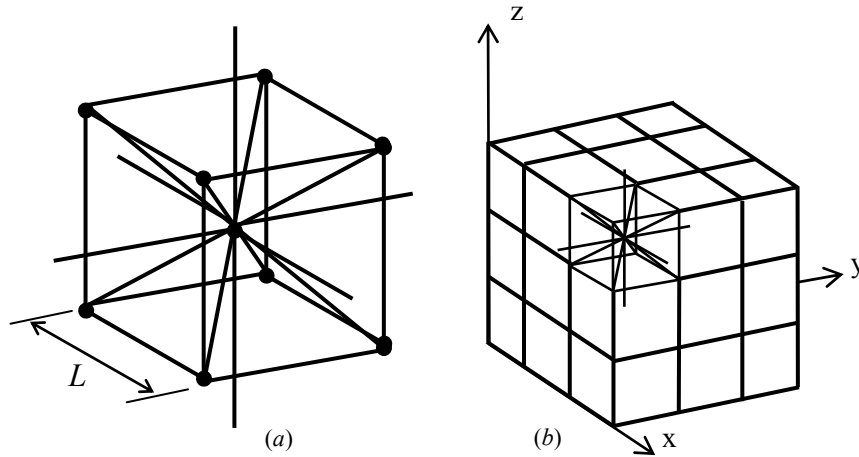

Figure 1. DEM discretization strategy: (a) basic cubic module, (b) generation of a prismatic body.

In case of an isotropic elastic material, the cross-sectional area A_l of the longitudinal elements (those defining the edges of the module and those parallel to the edges connected to the node located at the centre of the module) in the equivalent discrete model is:

$$A_l = \phi L^2 \tag{4}$$

where L is the length of the side of the cubic module under consideration. The function $\phi = (9+8\delta)/(18+24\delta)$, where $\delta = 9\nu/(4-8\nu)$, accounts for the effect of the Poisson's ratio ν. Similarly, the area A_d of the diagonal elements is:

$$A_d = \frac{2}{\sqrt{3}}\delta\phi L^2 \tag{5}$$

The coefficient $2/\sqrt{3}$ in equation (2) accounts for the difference in length between the longitudinal and the diagonal elements, this is, $L = 2/\sqrt{3} \cdot L_d$.

To arrive at expression of ϕ it is necessary to have equivalence between the isotropic elastic coefficient matrix and a computation of the equivalent directional properties of the bars as proposed by Nayfes Heftzy (1978).

It is important to point out that for $v = 0.25$, the correspondence between the equivalent discrete solid and the isotropic continuum is complete. On the other hand, discrepancies appear in the shear terms for values of $v \neq 0.25$. These discrepancies are small and may be neglected in the range $0.20 \leq v \leq 0.30$. For values outside this range, a different array of elements for the basic module should be used (see Nayfeh and Hefzy, 1978). It is interesting to note that while no lattice model can exactly represent a locally isotropic continuum, it can also be argued that no perfect locally isotropic continuum exists in practical engineering applications. Isotropy in solids is a bulk property that reflects the random distribution of the constituent elements orientation.

The equations of motion are obtained from equilibrium conditions of all forces acting on the nodal masses, resulting in a system of equations of the form:

$$\mathbf{M}\ddot{\mathbf{x}} + \mathbf{C}\dot{\mathbf{x}} + \mathbf{F}(t) - \mathbf{P}(t) = 0 \tag{6}$$

in which $\mathbf{x}$, $\dot{\mathbf{x}}$ and $\ddot{\mathbf{x}}$ denote vectors containing the nodal displacements, velocities and accelerations, respectively, while $\mathbf{M}$ and $\mathbf{C}$ are the mass and damping matrices, both are diagonals and the damping matrix is proportional only to the mass. The vectors $\mathbf{F}(t)$ and $\mathbf{P}(t)$ contain the internal and external nodal load.

Following the Courant-Friedrichs-Lewy criterion (see Bathe, 1996), the stability of the integration scheme is ensured by limiting the size of the time step. For the present implementation, the elements in the worst condition (this is, those requiring the smallest Δt) are the diagonal ones. Thus, considering the relationships in Equations (4) and (5), the limitation to the time increment is:

$$\Delta t \leq \frac{0.6L}{C_\rho} \tag{7}$$

where C_ρ is the longitudinal wave speed,

$$C_\rho = \sqrt{E / \rho} \tag{8}$$

The truss-like DEM has a natural ability to model cracks. They can be introduced into the models as pre-existent features and as the irreversible effect of crack nucleation and propagation. Pre-existent cracks are modeled using a simple strategy which consists in duplicate the nodes located on the crack surface together with the elimination of the elements connecting the material on both sides of the crack. This way, the DEM discretization is allowed to "open" along the crack locus, and pre-existent cracks are integrated seamlessly into the DEM formulation. Crack nucleation and propagation make use on non-linear constitutive models for material damage which allow the elements to break when they attain a critical condition. The details about the formulation and implementation of these non-linear constitutive models are given in the next section.

3.1 Non-linear constitutive models for material damage

Rocha *et al*. (1991) extended the lattice method here implemented (DEM) to model quasi brittle materials. To this end, they introduced the bilinear constitutive relationship illustrated in Figure 2. This constitutive law aims to capture the irreversible effects of crack nucleation and propagation by accounting for the reduction in the element load carrying capacity. The area under the force versus strain curve (the area of the triangle OAB in Figure 2) is the energy density necessary to fracture the area of influence of the element. Thus, for a given point P on the force vs. strain curve, the area of the triangle OPC represents the reversible elastic energy density stored in the element, while the area of the triangle OAP is the dissipated fracture energy density. Once the dissipated energy density equals the fracture energy, the element fails and loses its load carrying capacity. On the

other hand, in the case of compressive loads the material behaves as linear elastic. Thus, the failure in compression is induced by indirect traction. This assumption is reasonable for quasi-brittle materials for which the ultimate strength in compression is usually from five to ten times larger than that in tension (see Kupfer and Gerstle, 1973).
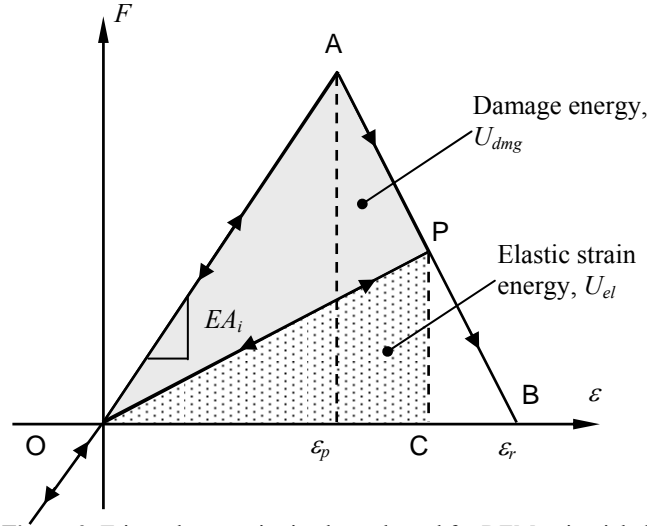

Figure 2. Triangular constitutive law adopted for DEM uni-axial elements.

Constitutive parameters and symbols in Figure 2 are (see Rocha *et al.*, 1991; and Riera and Rocha, 1991):

- *Force, F*: the element axial force as a function of the longitudinal strain ε.

- *Element area, A*: depending whether a longitudinal or a diagonal element is considered the values for A_l or A_d, see equations (4) and (5), should be adopted.

- *Element stiffness*: depending whether a longitudinal or a diagonal element is obtained multiplying the Young Modulus (*E*) by A_l or A_d, should be adopted.

- *Length of the DEM module, L.*

- *Specific fracture energy, G_f*: the fracture energy per unit area, which is coincident with the material fracture energy, G_c.

- *Equivalent fracture area, A_i^f*: this parameter enforces the condition that the energy dissipated by the fracture of the continuum material and its discrete representation are equivalent. With this purpose, a cubic sample with dimensions $L \times L \times L$ is considered. The energy dissipated when a continuum sample fractures into two parts due to a crack parallel to one of its faces is

$$\Gamma = G_f \Delta = G_f L^2 \qquad (9)$$

where Δ is the fracture area. By contrast, the energy dissipated when the DEM module fractures in two parts has to account for the contribution of five longitudinal elements (four coincident with the module edges and one internal one) and four diagonal elements, see Figure 1(a). Then, the energy dissipated by a DEM module can be written as follows

$$\Gamma_{\text{DEM}} = G_f \left(4\ 0.25\ c_A + c_A + 4\ c_A \left(\frac{2}{\sqrt{3}} \right)^2 \right) L^2 \qquad (10)$$

11

where the first term in the sum accounts for the four edge elements, the second term accounts for the internal longitudinal element, and the third term considers the contribution of the four diagonal elements. It is worth noting that the coefficient 0.25 in the first term accounts for the general case of an internal module with its four edge elements shared with four neighbors modules. When dealing with modules on the model surface, some of the edge elements could be shared by two elements or not shared at all. For such cases expression (10) has to be modified accordingly.

The coefficient c_A in equation (10) is a scaling parameter used to enforce the equivalence between Γ and Γ_{DEM}. Thus, equating expressions (9) and (10) results

$$G_f L^2 = G_f \left(\frac{22}{3} c_A \right) L^2 \tag{11}$$

from which it can be easily deduced that $c_A = 3/22$. Finally, the equivalent transverse fracture area of the longitudinal elements is

$$A_l^f = \left(3/22 \right) L^2 \tag{12}$$

while for the diagonal elements is

$$A_d^f = \left(4/22 \right) L^2 \tag{13}$$

- *Critical failure strain (ε_p)*: the maximum strain attained by the element before damage initiation (point A in Figure 2). The relationship between ε_p and the specific fracture energy, G_f, is given in terms of Linear Elastic Fracture Mechanics concepts. In this way

$$\varepsilon_p = R_f \sqrt{\frac{G_f}{E\left(1 - v^2\right)}} \tag{14}$$

where R_f is the so-called failure factor, which accounts for the presence of an intrinsic defect of size d. R_f is defined as

$$R_f = \frac{1}{Y\sqrt{d}} \tag{15}$$

where Y is a dimensionless parameter that depends on both the specimen and the crack geometry.

It is worth noting here that the intrinsic defect size, d, is predetermined, and it could be consider as a material property.

Any disorder in the material properties is introduced to the model by specifying a random distribution in the specific fracture energy, G_f.

- *Limit strain (ε_r)*: the strain value for which the element loses its load carrying capacity (point C in Figure 2). This value must be set to satisfy the condition that, upon the failure of the element, the dissipated energy density equals the product of the element influence area, A_i^f, times the specific fracture energy, G_f, divided by the element length. This is

$$\int_0^{\varepsilon_r} F(\varepsilon) d\varepsilon = \frac{G_f A_i^f}{L_i} = \frac{K_r \, \varepsilon_p^2 \, E \, A_i}{2} \tag{16}$$

in which the sub indexes i have to be specialized to l or d depending whether the element under consideration is a longitudinal or diagonal one, respectively.

The coefficient K_r in equation (16) is a function of the material properties and the element length, L_i. With equation (16), the expression for K_r can be retrieved:

$$K_r = \left(\frac{G_f}{E\varepsilon_p^2}\right)\left(\frac{A_i^f}{A_i}\right)\left(\frac{2}{L_i}\right)$$ (17)

In order to guarantee the stability of the algorithm, the condition $K_r \geq 1$ must be accomplished (Riera and Rocha, 1991). In this sense it is interesting to define the critical element length

$$L_{cr} = 2\left(\frac{G_f}{E\varepsilon_p^2}\right)\left(\frac{A_i^f}{A_i}\right)$$ (18)

The coefficient $\left(\frac{A_i^f}{A_i}\right)$ in equation (18) is $\left(\frac{A_l^f}{A_l}\right) = \frac{3}{22\phi}$ and $\left(\frac{A_d^f}{A_d}\right) = \frac{\sqrt{3}}{11\,\delta\phi}$ for the longitudinal and diagonal elements respectively (see equations (4), (5), (12) and (13)). In the special case of an isotropic continuum with $v = 0.25$, the value of the functions $\delta = 1.125$ and $\phi = 0.4$, which results in $\left(\frac{A_l^f}{A_l}\right) \approx \left(\frac{A_d^f}{A_d}\right) \approx 0.34$. Thus, for practical purposes a single value of the critical element length can be used for both the longitudinal and diagonal elements. Therefore, the above stability condition can be expressed as:

$$K_r = \frac{L_{cr}}{L_i} \geq 1 \quad \Rightarrow \quad L_i \leq L_{cr}$$ (19)

There is a maximum element length which preserves the stability of the element constitutive relationship.

Finally, the expression for the limit strain is

$$\varepsilon_r = K_r\varepsilon_p$$ (20)

It is interesting to note that in contrast to the usual practice in finite and boundary elements, the constitutive relationship in the DEM is not a function of the material properties only. The element constitutive relationship introduced above is defined in terms of parameters which are material properties (ε_p, E, R_{fc} and G_f), depend on model discretization (A_i^f and L) and depend on both, the material properties and the model discretization (E_i^A and ε_r). Besides, it is worth noting that although the DEM uses a scalar damage law to describe the uniaxial behavior of the elements, the global model accounts for anisotropic damage since it possesses elements orientated in different spatial directions. More sophisticated constitutive law that lets us incorporate more flexibility in the shape of the constitutive law and including plasticity discharge is published in Kosteski *et al.* (2011).

Studies about mesh convergence carried with DEM using mesh coarser that presented in the applications are shown in Kosteski *et al.* (2011), Miguel (2010). When we have interest in calibrating some problem it is necessary to adjust four parameters for a simple test that are, the global Elastic modulus (E), the density ρ, the G_f that is connected directly with the material toughness and the called critical strain ε_p connected with the strain in which the global model lives to be linear. If the model takes into account the random nature of the material, for example considering a G_f as random field, the characteristic of the distribution and its correlation length must be also furnished.

Another important feature of this approach is the assumption that G_f is a 3D random field with a Weibull probability distribution.

The local strain associated with maximum loading in each bar is called critical strain (ε_p). This value is also a random variable and its variability, which is measured using the coefficient of variation CV, is related to the G_f parameter by the following equation

$$CV(\varepsilon_p) = 0.5\, CV\,(G_f). \qquad (21)$$

The minimum value of ε_p determined in all the specimen bars is associated with the global strain for which a specimen loses linearity.

More exhaustive explanations of this version of the lattice model may be found in Kostesky (2011), (2012) Applications of the DEM in studies involving non-homogeneous materials subjected to fracture, such as concrete and rock, may be found in Riera and Iturrioz (1998), Dalguer *et al.* (2003)], Miguel *et al.* (2008), Iturrioz *et al.* (2009), and Miguel *et al.* (2010).

4. NUMERICAL AND EXPERIMENTAL RESULTS RELATED TO ACOUSTIC EMISSION

In the following, illustrative experimental results as well as numerical simulations of laboratory tests aimed at the determination of the *b* value on small scale rock or concrete samples are described in detail. Updated information on the fundaments and performance of the lattice formulation of the Discrete Element Method (DEM) proposed by Riera (1984), which was employed in the numerical analyses reported below, may be found in Kosteski *et al.* (2011). The study will focus on Accoustic Emmission (AE) tests reported by Carpinteri *et al.* (2009). The first test consists of a 160×160×500mm concrete prism subjected to uniaxial compression. The laboratory specimen was modeled by means of a 27×27×86 DEM cubic modules array, with the boundary conditions shown in Figure 5b. The parameters adopted in the DEM model are: Young´s modulus of the material E=9.0 GPa, mass density ρ=2500Kg/m2, mean value of the material toughness $\mu(G_f)$=560N/m and the linear elastic limit strain ε_p=2.4×10^{-4}. The random nature of the material is taken into account by assuming the toughness as a random field with a coefficient of variation CV= 0.5. The value of the concrete modulus E=9GPa was adopted on account of the fact that the test sample was subjected during 48 hours to a uniform compression load of 1300 kN, then unloaded. During the ensuing test the damaged specimen was reloaded up to its final collapse while monitored by AE sensors. Figure 5(b) shows the location of the AE sensor, at which accelerations in the direction normal to the specimen surface were computed employing the DEM.

The second example consists of a three point bending test. The concrete specimen dimensions were (80×150×700mm) with a 30mm pre-fissure length in the middle. The AE sensor was mounted as indicated by the gray box in Figure 6(b). Material properties were $E=35GPa$, ρ=2500Kg/m2, mean value of the toughness $\mu(G_f)$=130N/m and linear elastic limit strain ε_p=6.4×10^{-5}. Additional details concerning the experiments are given by Carpinteri *et al.* (2009, 2009b). Again, the non-homogeneous nature of concrete is taken into account in the numerical simulations by assuming that the toughness is a 3D random field with *CV*= 0.25, moreover the applied displacement rates on DEM models were reduced until no inertial effects could be detected in the output.

Figure 3 shows the load vs. time diagrams measured in the experiments and determined herein by numerical simulation. The peak loads and the areas under the curves are similar in both examples, except for the loss of linearity of the experimental curve for uniaxial compression near the peak load, which suggests that large damage occurred before the peak, effect that is not observed in the numerical analysis. The load vs. time diagrams of both controlled displacement tests are quite different: in the compression test an explosive collapse occurs, while in the three point bending test a softening branch after the peak load is reached can be seen. Figure 4 shows the

normalized energy balance in both tests determined by numerical simulation. In the uniaxial compression test, 95% of the external work is available in the form of elastic energy when the final collapse occurs, resulting in an explosive failure. On the other hand, in the three point bending test the external work is smoothly dissipated during the entire process and the available potential energy at the end of the test is not sufficient to produce an explosive collapse. Note that $E_{max}=U_e+U_k+U_d$ at t^*. In both examples, due to the slow rate of loading, the kinetic energy remains low throughout most of the test, although when collapse occurs under uniaxial compression, there is a sudden shift of elastic energy to kinetic energy. The final rupture configurations observed in the experimental setup and predicted numerically can be seen for the uniaxial compression test in Figure 5 and for the Three Point Bend test in Figure 6.
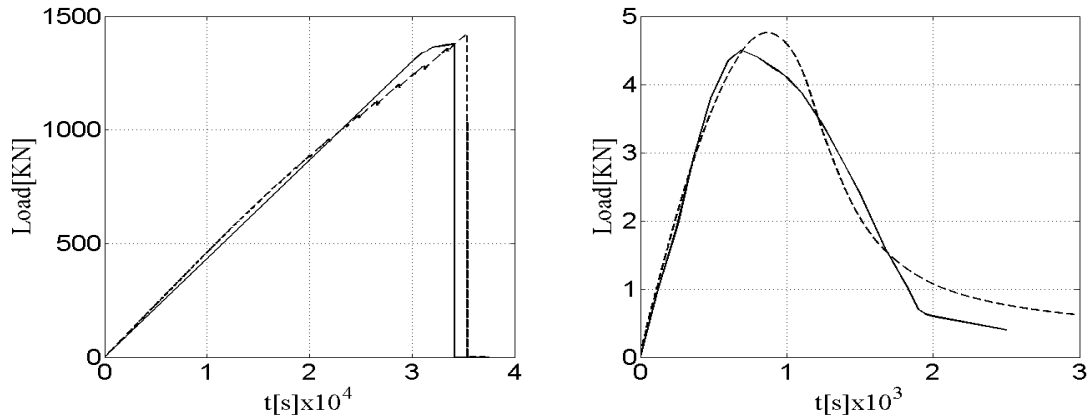

Figure 3. Load vs. time functions determined experimentally (continuous lines) and numerically (dashed lines): (a) Uniaxial compression test, (b) The three point bending test.

A summary of the numerical results concerning Acoustic Emission (AE) for both tests is presented next. They are considered as AE signal in the numerical simulation the normal surface acceleration in points localized on the specimen. Figure 7 shows the occurrence of individual AE events as vertical bars on the time axis. The height of each bar is proportional to the intensity of the event, registered on the sample surface. The figure also shows the total load vs. time curves on the samples. Histograms of the number of AE events and the evolution with time of the accumulated number of events are shown in Figure 8 for the uniaxial compression test and for the three points bending test. Finally Figure 9 shows the relations between the number of AE events and their magnitudes in logarithmic scale. Straight lines were fitted to the simulated data within selected time intervals, as indicated in the graphs. The magnitude scale was normalized. All the signals utilized for the b-values calculation in the numerical simulation had higher amplitudes than the fixed threshold A_{thres}. For this reason, only few events were identified in the simulation (about 200 in each example). By decreasing even further the displacement rate and adoting a lower threshold, it would be possible to identify more AE peaks, thus increasing the sample size, but the extension of the analysis was considered unnecessary. The values of b computed in both examples are compatible with the values determined experimentally by Carpinteri *et al.* (2009, 2009b). In addition, the numerical simulations reproduced the tendency observed in laboratory experiments, which show that b decreases towards values around unity as the degree of damage increases. Note that in the uniaxial compression test the b value was observed to decrease from 1.69 to 1.19, while according to DEM predictions it decreases from 1.47 to 1.16. In the laboratory bending test, b decreases from 1.49 to 1.11, while the numerical simulation predicts a decrease from 1.10 to 1.03.
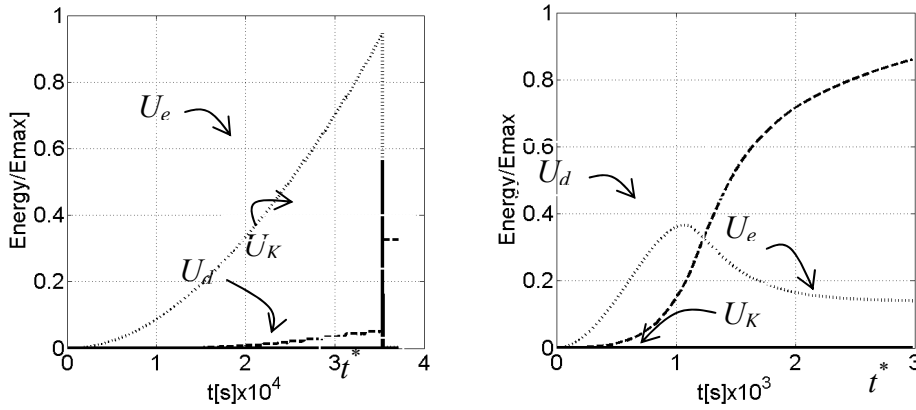
Figure 4. Energy balance vs time (U_e= elastic energy, U_k= kinetic energy, U_d= dissipated energy (a) Uniaxial compression (E_{max}=4888Nm), (b) Three point bending (E_{max}=0.65Nm).
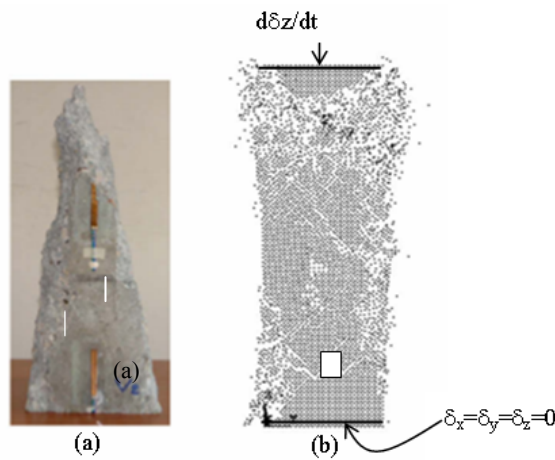

Figure 5. (a) Final rupture configuration of concrete specimen subjected to uniaxial compression (Carpinteri *et al.*, 2009) and (b) collapse configuration predicted by DEM model after peak load is reached (only nodal masses are shown). The white rectangle indicates the position of the sensor.

Finally Figure 10 presents plots of the logarithm of the number of events larger than given amplitudes vs. the logarithms of the amplitudes for the DEM simulations of the compression test (left plot) and of the three points bending test (right plot). Notice that the shape of these curves are similar to the typical curve for seismic data shown in Figure 3, which according to Scholz (2002), from the size distribution of subfaults, may be expected to present slopes given by b_1= ⅔ and b_2= 1. While similar values are usually found in actual seismic records for specific faults or seismic regions, they differ from some of the laboratory or numerical simulations results for small samples discussed herein.
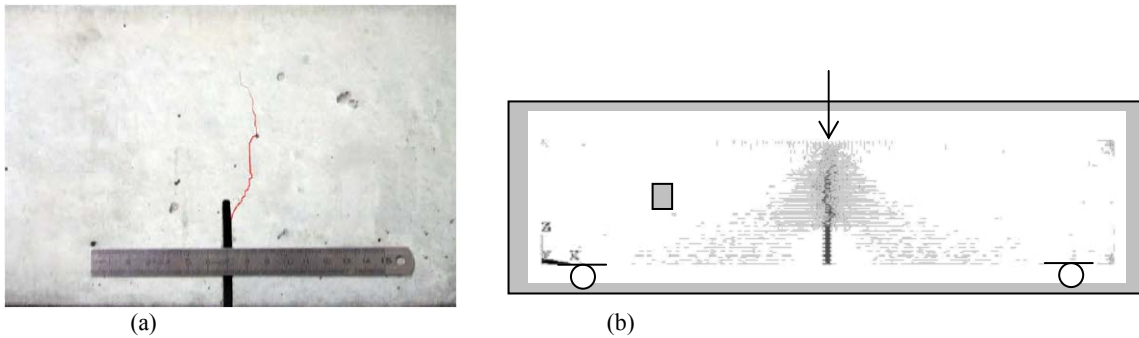
Figure 6. (a) Detail of the exerimental rupture configuration of the specimen subjected to Three Point Bending (Carpinteri *et al.*, 2009a) (b) Numerical rupture configuration according to DEM (only damaged bars are plotted). The small gray rectangle indicates the position of the sensor.
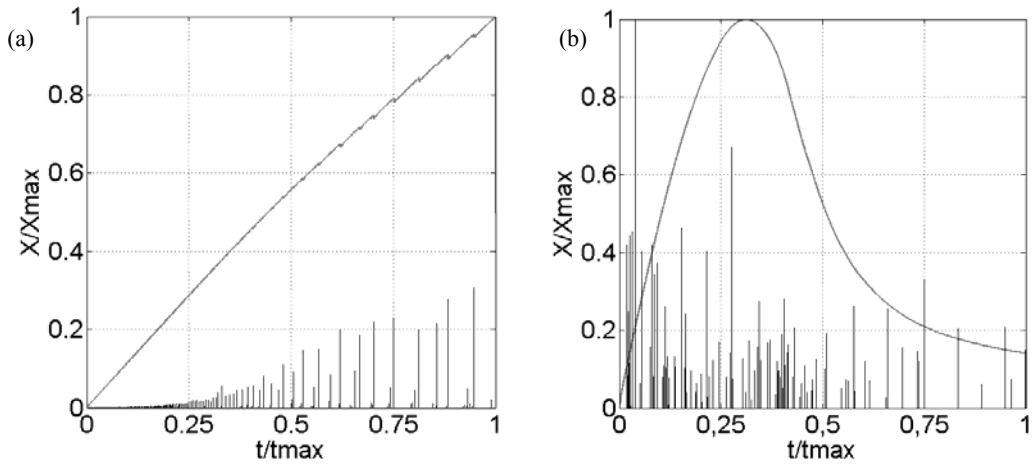
Figure 7. The continuous curves indicate the total load in the DEM models, while the bars show the amplitudes of AE events. Both axis were normalized to the maximum value. (a) Uniaxial compression test, (b) Three points bending test.
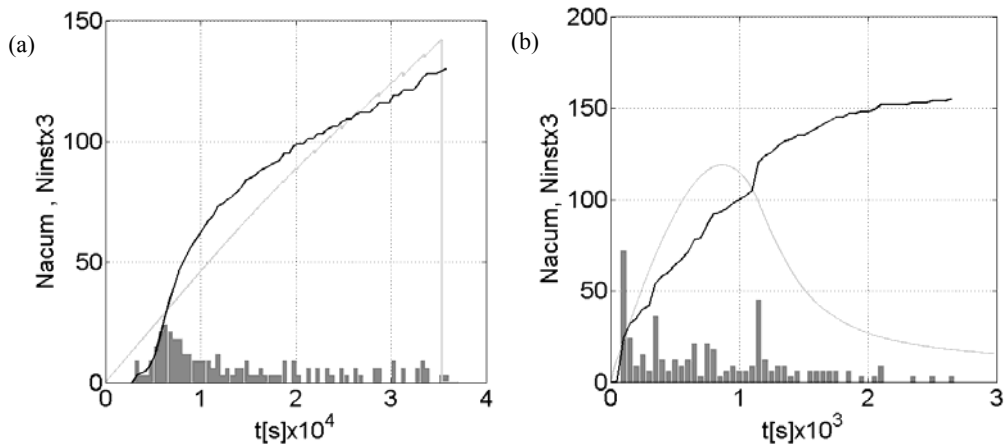

Figure 8. Histograms of the number of AE events and evolution with time of the accumulated number of AE events (thich line) and loas evolution (thin line) for: (a) Uniaxial compression test, (b) Three points bending test.

5. CONCLUSIONS

In this work, two experimental tests carried out on concrete specimens loaded up to failure are analyzed. One was a prismatic specimen subjected to uniaxial compressive loading, the other was a pre-cracked beam subjected to the three point bending test. For both examples experimental and numerical results are presented. The numerical simulations were performed using a version of the truss-like Discrete Element Method (DEM). During the tests, the Acoustic Emission (AE) technique was used to monitor the damage process taking place in the specimens. The numerical and experimental results obtained in the two examples are compared, and their intrinsic differences are identified.
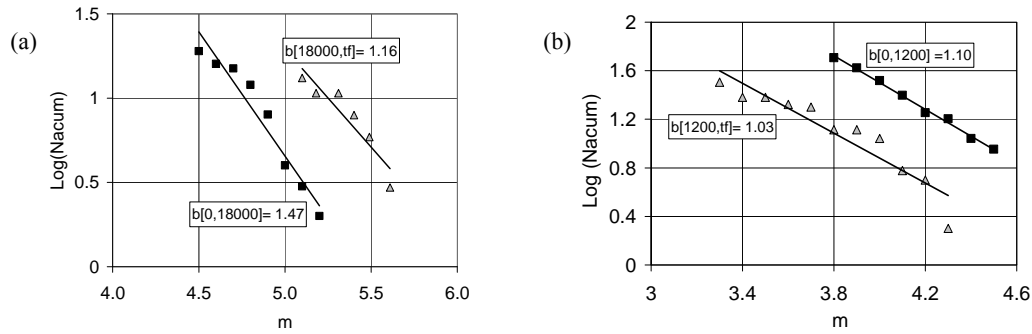
Figures 9. Determination of *b* - coefficients for simulated response in (a) uniaxial compression test and (b) three point bending test. The time intervals intervals used in the computation of *b* values are indicated between brackets.
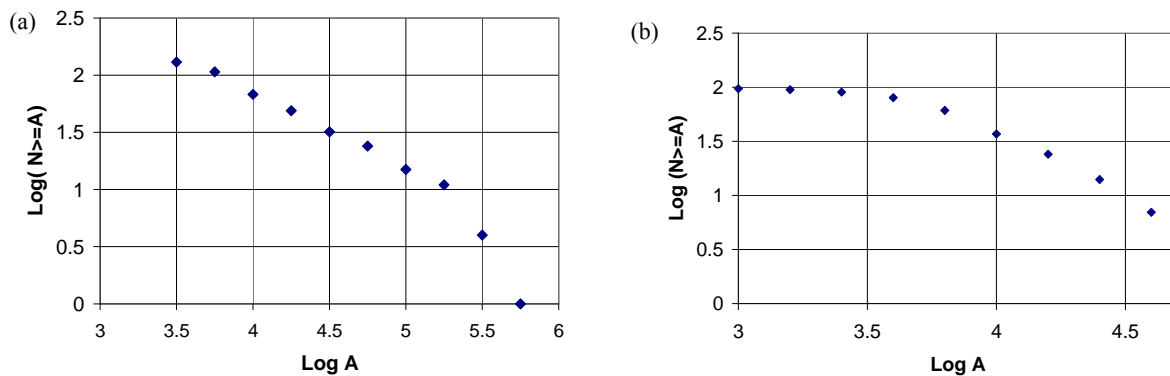
Figure 10. plots of the logarithm of the number of events with amplitudes larger than A vs. the logarithm of A for the DEM simulations of compression (left) and of three points bending (right). The *b* values in the high magnitudes regions are b_2= 2.40 (compression) and b_2= 1.16 (bending).

From these analyses, the following conclusions may be drawn.

-   The comparison between the experimental and numerical results shows reasonable correlations, for both examples, in terms of conventional results, such as load vs. time and final configurations.

-   In terms of the distribution of AE event amplitudes in time, the results were seen to be consistent, and any differences observed between the experimental and numerical results were accounted for. It is important to point out that the numerical *b*-values obtained are compatible with the experimental values and in good agreement with damage theories (Carpinteri et. al. (2009)), showing a tendency to decrease during the damage process.

-   The low number of AE events analyzed in the numerical simulations (fewer than 200 events in both cases) compared with the number determined by AE monitoring is an issue to be discussed in detail in relation to the results obtained. However, the aim of these numerical simulations, as mentioned above, was to identify the general trends on a preliminary base. To increase the number of AE events analyzed in the numerical simulations you need a finer discretization, something we shall do after this initial exploration of the applicability of DEM simulations to this kind of process.

-   This study has shown the potential applications of the truss-like Discrete Element Method (DEM) not only to simulate AE monitoring analysis, but also to provide a better understanding of the relationships between the basic AE parameters.

REFERENCES

Aki, K.: Scaling law of seismic spectrum. *J. Geophys. Res.* 1967; 72, 1217-1231.

Bathe KJ (1996) Finite element procedures. Prentice-Hall, Inc., New Jersey.

Carpinteri A.: Scaling laws and renormalization groups for strength and toughness of disordered materials. *Int J Solid Struct* 1994; 31:291–302.

Carpinteri A., Lacidogna G., Niccolini G., Puzzi S.: Critical defect size distributions in concrete structures detected by the acoustic emission technique. *Meccanica* 2008; 43: 349–63.

Carpinteri A., Lacidogna G., Niccolini G.: Fractal analysis of damage detected in concrete structural elements under loading. Chaos, *Solitons and Fractals* 2009; 42: 2047–2056.

Carpinteri A., Lacidogna G., Puzzi S.: From criticality to final collapse: evolution of the b-value from 1.5 to 1.0. *Chaos Soliton Fract* 2009; 41:843–853.

Chakrabarti B. K., Benguigui L. G.: *Statistical Physics of Fracture and Breakdown in Disordered Systems*. Clarendon Press, Oxford, 1997.

Dalguer L. A., Irikura K., Riera, J. D.: Simulation of tensile crack generation by three-dimensional dynamic shear rupture propagation during an earthquake. *J. Geophys. Res.* 2003; 108(B3): 2144.

Iturrioz I., Miguel L. F. F., Riera J. D.: Dynamic fracture analysis of concrete or rock plates by means of the Discrete Element Method. *Latin American Journal of Solids and Structures* 2009; 6: 229–245.

Kosteski L., Iturrioz I., Batista R.G., Cisilino A. P.: The truss-like discrete element method in fracture and damage mechanics. *Engineering Computations*, 2011; 6: 765–787.

Kosteski, L.E.; Barrios, R.; Iturrioz, I.: Crack propagation in elastic solids using the truss-like discrete element method. Int J Fract, 2012;DOI 10.1007/s10704-012-9684-4.

Nayfeh A.H., Hefzy M. S.: Continuum modeling of three-dimensional truss-like space structures. *AIAA Journal*, 1978; 8:779–787.

Kupfer HB, Gerstle KH (1973) Behaviour of concrete under biaxial stresses. *Journal of the Engineering Mechanics Division, American Society of Civil Engineers*, 99:853-866.

Miguel L. F. F., Iturrioz I., Riera J.D.: Size effects and mesh independence in dynamic fracture analysis of brittle materials. *Computer Methods Modeling in Engineering & Sciences*, 2010; 56:1-16.

Miguel, L. F. F., Riera, J. D., and Iturrioz, I.: Influence of size on the constitutive equations of concrete or rock dowels. *International Journal for Numerical and Analytical Methods in Geomechanics* 2008; 32: 1857–188.

Pollock A. A.: *Acoustic emission-2: acoustic emission amplitudes. Non-Destruct. Test* 1973;6: 264–9.

Richter C. F.: *Elementary Seismology*. W. H. Freeman, San Francisco and London, 1958.

Riera J. D.: Local effects in impact problems on concrete structures. Proceedings, *Conference on Structural Analysis and Design of Nuclear Power Plants*, Porto Alegre, RS, Brazil, 1984; Vol. 3, CDU 264.04:621.311.2:621.039.

Riera JD, Rocha MM (1991) A note on the velocity of crack propagation in tensile fracture. *Revista Brasileira de Ciencias Mecânicas*, 12/3:217-240.

Riera J.D., Iturrioz I: Discrete element model for evaluating impact and impulsive response of reinforced concrete plates and shells subjected to impulsive loading. *Nuclear Engineering and Design*, 1998; 179: 135-144.

Rocha MM, Riera JD, Krutzik NJ (1991) Extension of a model that aptly describes fracture of plain concrete to the impact analysis of reinforced concrete. In: *International Conference on Structural Mechanics Reactor Technology* (SMIRT 11), Tokyo, Japan.

Rundle J., Turcotte D., Shcherbakov R., Klein W., Sammis, C.: Statistical physics approach to understanding the multiscale dynamics of earthquake fault systems. *Reviews of Geophysics* 2003; 4: 8755–1209.

Scholz, C.H.: *The Mechanics of Earthquakes and Faulting*, 2002; 2nd. Edition, Cambridge University Press.

Turcotte D. L., Newman W.I., Shcherbakov R.: Micro and macroscopic models of rock fracture. *Geophys J. Int*. 2003; 152:718–28.